

Bilevel Integrative Optimization for Ill-posed Inverse Problems

Risheng Liu, *Member, IEEE*, Long Ma, Xiaoming Yuan, Shangzhi Zeng, and Jin Zhang

Abstract—Classical optimization techniques often formulate the feasibility of the problems as set, equality or inequality constraints. However, explicitly designing these constraints is indeed challenging for complex real-world applications and too strict constraints may even lead to intractable optimization problems. On the other hand, it is still hard to incorporate data-dependent information into conventional numerical iterations. To partially address the above limits and inspired by the leader-follower gaming perspective, this work first introduces a bilevel-type formulation to jointly investigate the feasibility and optimality of nonconvex and nonsmooth optimization problems. Then we develop an algorithmic framework to couple forward-backward proximal computations to optimize our established bilevel leader-follower model. We prove its convergence and estimate the convergence rate. Furthermore, a learning-based extension is developed, in which we establish an unrolling strategy to incorporate *data-dependent network architectures* into our iterations. Fortunately, it can be proved that by introducing some mild checking conditions, all our original convergence results can still be preserved for this learnable extension. As a nontrivial byproduct, we demonstrate how to apply this *ensemble-like methodology* to address different low-level vision tasks. Extensive experiments verify the theoretical results and show the advantages of our method against existing state-of-the-art approaches.

Index Terms—Bilevel optimization, Global convergence, Low-level vision.

1 INTRODUCTION

INVERSE problems naturally occur in almost all the areas of science and engineering [1], [2]. This problem can be formulated using an analytical description $\mathcal{A} : \mathcal{X} \rightarrow \mathcal{Y}$ of the forward operator in some given vector spaces \mathcal{X} and \mathcal{Y} . For example, typical tasks in computer vision that can be phrased as inverse problems include image deblurring, where \mathcal{A} is the blur kernel, super-resolution, where \mathcal{A} downsamples high-resolution images, or image inpainting, where \mathcal{A} is given by a mask corresponding to the inpainting domain. In medical imaging, common forward operators \mathcal{A} are the Fourier transform in MRI and the ray transform in CT. In this way, the target of inverse problems is to obtain an unknown \mathbf{x}^* from the given noisy observation $\mathbf{y} \sim \mathcal{A}(\mathbf{x}^*)$. However, in most real-world scenarios, the above problem is always ill-posed, that is, the solution either not exists, is not unique or does not depend continuously on the datum \mathbf{y} . Therefore, the scope of this work is to investigate the so-called Ill-posed Inverse Problems (IIPs for short). In the past years, a variety of approaches have been proposed to address IIPs.

The first category of methods aim to find the maximum likelihood solution, resulted in the minimization of the data

discrepancy [3], [4]. To penalize the unfeasible solutions, different variational regularizations have been developed to encode prior information about \mathbf{x}^* and they actually seek to minimize the regularized objective functionals [5]. These energy minimization approaches can be applied to solve various types of IIPs, but they often have poorer performance on an individual task. This is mainly because it is very hard to design correct priors to appropriately fit our desired solutions in real-world problems.

A more recent trend is to establish regression-type neural networks to learn a direct inverse mapping \mathcal{A}^\dagger from the observation space \mathcal{Y} to the solution space \mathcal{X} [6], [7], [8]. Such methods have achieved impressive performance in some practical applications. While the obvious disadvantages with these learned deep approaches are that their performances completely depend on rich high-quality training data and it is also challenging to learn a single network to address various different tasks. Theoretically, it is extremely hard to understand and interpret these complex network structures, due to their heuristic nature. Very recently, preliminary works have begun to link conventional approaches with task-specific computational modules (e.g., deep learning architectures) and developed a series of optimization-inspired learning methods to solve IIPs [9], [10]. The idea is to unroll an existing optimization process and replace the explicit iterative updating rule with hand-designed operators and/or learned architectures [11]. Unfortunately, due to the uncontrolled inexact computational modules, it is hard to theoretically guarantee the convergence of these methods. The works in [10], [12], [13] tried to introduce error control rules to correct improper modules and thus prove the convergence of their trained iterations. However, these additional error checking process will slow down the particular computation when handling challenging prob-

- R. Liu and L. Ma are with the DUT-RU International School of Information Science & Engineering, Dalian University of Technology, and also with the Key Laboratory for Ubiquitous Network and Service Software of Liaoning Province, Dalian 116024, China. E-mail: rslu@dlut.edu.cn, malone94319@gmail.com.
- X. Yuan and S. Zeng are with Department of Mathematics, The University of Hong Kong, Hong Kong. E-mail: xmyuan@hku.hk, zengsz@connect.hku.hk.
- J. Zhang is with Department of Mathematics, Southern University of Science and Technology, Shenzhen 518055, China. E-mail: zhangj9@sustech.edu.cn.

Manuscript received xxxx.

lems. Moreover, deeper theoretical investigations (e.g., the stability of the iterations) are still missing.

1.1 Our Contributions

In this work, we propose a completely new paradigm, named Bilevel Integrative Optimization (BIO), to formulate and optimize IIPs in knowledge and data collaboration manner. Different from traditional variational modeling techniques, which only consider a single energy formulation, we introduce a specific bilevel system¹ to combine principled energies, hand-designed priors and even deeply trained network architectures to formulate IIPs. Since in BIO we consider general convex composite (not necessarily smooth) energies in both upper and lower subproblems, to our best knowledge, no existing bilevel optimization algorithms can be used to address the resulted optimization problem. Fortunately, by re-characterizing the latent feasibility as explicit set constraints, an efficient iteration scheme is developed to address BIO. Theoretically, we can prove that our established iteration scheme can strictly converge to the global optimal solution of BIO. We also show that the computational errors during our practical iterations can be successfully dominated, thus verify the stability of the proposed method. Extensive experiments on real-world computer vision applications finally demonstrate the efficiency and effectiveness of the proposed framework. In summary, our contributions mainly include:

- As a new modeling paradigm, BIO provides a flexible and modularized framework to integrate principled energies, hand-designed priors and deeply trained network architectures to formulate IIPs.
- By investigating the stability of the nested lower-level subproblem, the validity of our latent feasibility re-characterization based single level reformulation scheme is strictly convinced.
- Different from existing convex bilevel methods (e.g., [15], [16], [17]), which is only applicable for strongly convex upper-level subproblem, our solution scheme can successfully handle models with more general convex upper-level objectives.

2 RELATED WORK

2.1 Existing Approaches for Inverse Problems

The most widely used approaches in solving IIPs are to minimize the mass-fit against data, i.e., where the generalized inverse A^\dagger is unbounded. Unfortunately, these purely analytic models are typically just an approximation to these real-world tasks. Moreover, given no presumption about the nature of the solution (e.g., the statistics of the image), it is virtually impossible to solve the IIPs, especially in real scenarios.

Over the past decades, one of the most widely used way to approach IIPs is by defining a likelihood and prior, and optimizing for the Maximum A Posteriori (MAP) solution. The sparsity of natural images is commonly utilized for

defining the priors in some primitive works [3]. The non-local self-similarity is then developed for constructing the priors [18]. As further research, researchers tend to design complicated priors for the competitive performance [4], [5]. While more expressive priors allow for better representation of the signal of interest, they will typically make optimization more difficult. In fact, only for a few trivial prior-likelihood pairs will inference remain convex. In practice, one often has to resort to approximations of the objective and to approximate double-loop algorithms in order to allow for scalable inference.

The huge field of machine learning provides several data-driven approaches to tackle these problems by using training datasets to either construct a problem adapted forward operator and use an established inversion method or to solve the inverse problem directly [19], [20]. In particular, deep learning approaches using neural networks with multiple internal layers have become popular over the recent few years [21]. The development of deep learning lies in the massive data [22] and the significant network architecture [23]. Nowadays, the large scale of data has been seen everywhere. Consequently, the design of architecture plays a decisive role to push forward deep learning. Indeed, the big advancements of deep learning owing to some targeted design of architecture [8], [24]. There is no denying that the tremendous success of deep learning has achieved in many fields. But it is a vital shortcoming that the distribution of training set directly decide the performance in test data. Moreover, no consistent mathematical theory on deep neural networks for inverse problems has been developed yet besides the stunning experimental results, which have been published so far for many different types of applications to inverse problems.

Some recent works put more emphasis on building the connection between with traditional optimization and learning architecture. One is to design the complex priors with learning parameters and unrolling the iteration scheme to obtain the end-to-end learned architecture [25], [26]. The other is to substitute the subproblem with the data-driven network in the optimization process [11], [27]. To be brief, the key intentions of such methods lie in how to derive the learned architecture from the optimization model to incorporate the data prior. But unfortunately, the convergence behaviors and stability properties become difficult to analyze although the performances indeed bring the advancements, which loses the strengths of traditional optimization. There exists some works [10] have presented the convergence analysis by introducing the error control rules, which bring the extra computational burden and the theoretical results are not satisfied.

2.2 Bilevel Optimization Techniques

In general, bilevel models are hierarchical optimization problems, where the feasible region of the upper-level subproblem is restricted by the graph of the solution set mapping of the lower-level subproblem, see, e.g., [28]. Due to the coupling of the hierarchical subproblems, it is indeed extremely challenging to optimize classic bilevel problems. Recently, a series of works [15], [16], [17] have tried to address specific bilevel models, in which they minimize

1. Please notice that our BIO formulation is actually not a standard bilevel programming with coupled variables, but a specific case with one single variable [14].

a convex function over the set of constrained minimizers of another convex function. Although upper-level variables exactly coincide with lower-level variables, the resulted convex bilevel problems are still extraordinarily ill-posed. The early work in [15] considered this category of models with both smooth upper and lower subproblems. Recent works in [16], [17] introduced minimal norm gradient and sequential averaging methods to address convex bilevel problems with strongly convex and smooth upper-level subproblem. Unfortunately, the problem settings in [15], [16], [17] are too restrictive for our tasks. Thus neither of these schemes is amenable as a solution method for the optimization problem in this work.

3 THE PROPOSED FRAMEWORK

In this section, we establish a generic convex bilevel framework to integrate different categories of information to formulate and optimize challenging inverse problems².

3.1 Bilevel Integration Modeling

We first consider a composite optimization formulation:

$$\min_{\mathbf{x}} \Psi(\mathbf{x}) := \psi(\mathbf{x}) + \varphi(\mathbf{x}), \quad (1)$$

where ψ, φ are extended-valued convex functions $\mathbb{R}^n \rightarrow (-\infty, \infty]$ and φ may be possibly nonsmooth. The model in Eq. (1) has drawn increasing attention recently for the emerging applications in leaning and vision areas, e.g., face recognition [29], saliency detection [30], image restoration [10], optical flows [25] and many others [31]. While different from these existing approaches, which just formulate their objectives as specific forms of Eq. (1), here we would like to consider the solution set of Eq. (1) as the lower-level latent feasibility of our task and actually aim to solve the following bilevel problem with hierarchy

$$\min_{\mathbf{x}} F(\mathbf{x}) := f(\mathbf{x}) + g(\mathbf{x}), \text{ s.t. } \mathbf{x} \in \arg \min_{\mathbf{x}} \Psi(\mathbf{x}), \quad (2)$$

where we introduce another composite function F as our upper-level objective. Similarly, we also assume that both f, g are also extended-valued convex functions $\mathbb{R}^n \rightarrow (-\infty, \infty]$ and g may be possibly nonsmooth. In this way, we actually obtain a convex bilevel optimization model, which implicitly integrate two different hierarchies of information (i.e., F and Ψ) for IIPs modeling.

3.2 A New Single Level Reformulation Strategy

From an optimization perspective, we actually utilize the lower-level subproblem Eq. (1) to characterize the feasible region of BIO in Eq. (2). The main benefit of such strategy is that we can take full advantage of our domain knowledge of the task. Indeed, Eq. (2) can be recognized as a specific convex bilevel model. However, both upper and lower levels are in general lack of smoothness and strong convexity. Thus the existing solution schemes [15], [16], [17] no longer admit any theoretical validity. In fact, when the upper-level subproblem is in the absence of strong convexity, directly

solving Eq. (2) with such latent feasibility is extremely challenging.

Motivated by the observation that in applications, the latent feasibility in Eq. (1) usually possesses some underlying structures, in this paper, we develop a new optimization strategy with solid theoretical guarantees for structural BIO. In particular, we re-characterize the latent feasibility in Eq. (1). Therefore we shall reformulate Eq. (2) in terms of the re-characterization of Eq. (1) into a standard optimization problem which is numerically trackable. To this end, we first list some structural assumptions, which are necessary for our following analysis and easily to satisfy in applications of practical interests. Specifically, throughout this present paper, we suppose that ψ takes the form that $\psi(\mathbf{x}) = h(\mathcal{A}(\mathbf{x}))$, where \mathcal{A} is some given linear operator and h has the following structural properties³

Assumption 1. *Function h is closed, proper, convex and admits the properties that (i) h is continuously differentiable on $\text{dom}h$, assumed to be open, and (ii) h is strongly convex on any compact convex subset of $\text{dom}h$.*

We are now ready to state the following theorem to investigate the feasibility of our problem.

Theorem 1. (latent feasibility re-characterization) *Let \mathcal{X} be the solution set of Eq. (1) (i.e., $\mathcal{X} := \arg \min_{\mathbf{x}} \Psi(\mathbf{x})$), then \mathcal{A} is invariant on \mathcal{X} . That is, given any $\bar{\mathbf{x}} \in \mathcal{X}$, \mathcal{X} can be explicitly characterized as*

$$\mathcal{X} = \{\mathbf{x} | \mathcal{A}(\mathbf{x}) = \mathcal{A}(\bar{\mathbf{x}}), \varphi(\mathbf{x}) \leq \varphi(\bar{\mathbf{x}})\}. \quad (3)$$

Please notice that the proofs of all our theoretical results are presented in Appendix.

Following Theorem 1, we define $\mathcal{X}_\varphi := \{\mathbf{x} | \varphi(\mathbf{x}) \leq \varphi(\bar{\mathbf{x}})\}$ and $\bar{\mathbf{y}} = \mathcal{A}(\bar{\mathbf{x}})$. Then the original bilevel model in Eq. (2) can be equivalently reformulated as the following single-level constrained optimization problem:

$$\min_{\mathbf{x}} f(\mathbf{x}) + g(\mathbf{x}) + \iota_{\mathcal{X}_\varphi}(\mathbf{x}), \text{ s.t. } \mathcal{A}(\mathbf{x}) = \bar{\mathbf{y}}, \quad (4)$$

where $\iota_{\mathcal{X}_\varphi}$ denotes the indicator function of \mathcal{X}_φ . Now the problem of solving BIO is reformulated to the single level standard optimization Eq. (4). In order to solve the single level reformulation, we introduce the following augmented Lagrangian function with auxiliary variables \mathbf{s}, \mathbf{z}

$$\begin{aligned} \mathcal{L}_\beta(\mathbf{x}, \mathbf{z}, \mathbf{s}, \{\boldsymbol{\lambda}_i\}_{i=1}^3) &:= f(\mathbf{x}) + g(\mathbf{z}) + \iota_{\mathcal{X}_\varphi}(\mathbf{s}) \\ &+ \langle \boldsymbol{\lambda}_1, \mathbf{z} - \mathbf{x} \rangle + \langle \boldsymbol{\lambda}_2, \mathbf{s} - \mathbf{x} \rangle + \langle \boldsymbol{\lambda}_3, \mathcal{A}(\mathbf{x}) - \bar{\mathbf{y}} \rangle \\ &+ \frac{\beta}{2} (\|\mathbf{z} - \mathbf{x}\|^2 + \|\mathbf{s} - \mathbf{x}\|^2 + \|\mathcal{A}(\mathbf{x}) - \bar{\mathbf{y}}\|^2), \end{aligned}$$

where $\{\boldsymbol{\lambda}_i\}_{i=1}^3$ denote the dual multipliers and $\beta > 0$ denotes the penalty parameter. Then the proximal ADMM

3. Some commonly used functions in learning and vision (e.g., linear regression $h(\mathbf{z}) = \frac{1}{2} \|\mathbf{z} - \mathbf{b}_1\|^2$, logistic regression $h(\mathbf{z}) = \sum_{i=1}^m \log(1 + e^{\mathbf{z}^i}) - \langle \mathbf{b}_2, \mathbf{z} \rangle$ and likelihood estimation under Poisson noise $h(\mathbf{z}) = -\sum_{i=1}^m \log(\mathbf{z}_i) + \langle \mathbf{b}_3, \mathbf{z} \rangle$) automatically satisfy these assumptions, where $\mathbf{b}_1, \mathbf{b}_2$ and \mathbf{b}_3 are parameters.

2. We will demonstrate how to apply our framework to integrate both knowledge and data for real-world applications in Sec. 5.

(with $\tau > 0$) reads as follows:

$$\left\{ \begin{array}{l} \mathbf{z}^{k+1} \in \arg \min_{\mathbf{z}} \mathcal{L}_{\beta}(\mathbf{x}^k, \mathbf{z}, \mathbf{s}^k, \{\lambda_i^k\}_{i=1}^3) \\ \quad + \frac{\tau}{2} \|\mathbf{z} - \mathbf{z}^k\|^2, \\ \mathbf{s}^{k+1} \in \arg \min_{\mathbf{s}} \mathcal{L}_{\beta}(\mathbf{x}^k, \mathbf{z}^k, \mathbf{s}, \{\lambda_i^k\}_{i=1}^3) \\ \quad + \frac{\tau}{2} \|\mathbf{s} - \mathbf{s}^k\|^2, \\ \mathbf{x}^{k+1} \in \arg \min_{\mathbf{x}} \mathcal{L}_{\beta}(\mathbf{x}, \mathbf{z}^{k+1}, \mathbf{s}^{k+1}, \{\lambda_i^k\}_{i=1}^3) \\ \quad + \frac{\tau}{2} \|\mathbf{x} - \mathbf{x}^k\|^2, \\ \lambda_1^{k+1} = \lambda_1^k + \beta(\mathbf{z}^{k+1} - \mathbf{x}^{k+1}), \\ \lambda_2^{k+1} = \lambda_2^k + \beta(\mathbf{s}^{k+1} - \mathbf{x}^{k+1}), \\ \lambda_3^{k+1} = \lambda_3^k + \beta(\mathcal{A}(\mathbf{x}^{k+1}) - \bar{\mathbf{y}}). \end{array} \right. \quad (5)$$

Thanks to Theorem 1, we directly have a corollary to guarantee the convergence of Eq. (5) toward the global optimal solutions of Eq. (2).

Corollary 1. *Suppose that the problem in Eq. (4) has KKT solutions. Let $\{(\mathbf{x}^k, \mathbf{z}^k, \mathbf{s}^k, \lambda^k)\}$ be the sequence generated by Eq. (5) on problem (4), then $\{(\mathbf{x}^k, \mathbf{z}^k, \mathbf{s}^k, \lambda^k)\}$ converges to the KKT point set of Eq. (4). In particular, the sequence $\{\mathbf{x}^k\}$ converges to the global optimal solutions of Eq. (2).*

Remark 1. *Indeed, we can further estimate a nice linear convergence rate of Eq. (5) for particular models. That is, if we have that f takes the form that $f(\mathbf{x}) = h(\tilde{A}\mathbf{x})$ where \tilde{A} is some given linear operator, h satisfies Assumption 1, g represents (1) convex polyhedral regularizer; (2) group-lasso regularizer; (3) sparse group lasso regularizer, ψ is a convex polyhedral function, then $\{(\mathbf{x}^k, \mathbf{z}^k, \mathbf{s}^k, \lambda^k)\}$ converges linearly to the KKT point set of problem in Eq. (4). In particular, the sequence $\{\mathbf{x}^k\}$ converges linearly to the global optimal solutions of Eq. (2).*

4 THEORETICAL INVESTIGATIONS

With Theorem 1, we have that the solutions returned by solving Eq. (4) can exactly optimize the bilevel problem in Eq. (2). It can be seen that our single-level reformulation based optimization scheme heavily relies on the solution set re-characterization. In particular, we require one solution of the lower-level subproblem (i.e., $\bar{\mathbf{x}} \in \arg \min_{\mathbf{x}} \psi(\mathbf{x}) + \varphi(\mathbf{x})$) to establish the feasible set \mathcal{X} .

However, in general, obtaining such exact solution is intractable. That is, we in practice can only calculate a solution with errors for the lower-level subproblem in Eq. (1), i.e., obtain a point $\bar{\mathbf{x}}_{\delta}$ satisfying $d(\bar{\mathbf{x}}_{\delta}, \mathcal{X}) \leq \delta$, where d is the distance mapping, $\delta \geq 0$ measures the computational errors and \mathcal{X} denotes the solution set of the lower-level subproblem (defined in Eq. (3)). As a consequence, we actually should consider the practical optimization process of Eq. (2) as solving an approximation of Eq. (4), which can be formulated as follows⁴:

$$\min_{\mathbf{x}} F(\mathbf{x}), \text{ s.t. } \mathcal{A}(\mathbf{x}) = \mathcal{A}(\bar{\mathbf{x}}_{\delta}), \varphi(\mathbf{x}) \leq \varphi(\bar{\mathbf{x}}_{\delta}). \quad (6)$$

In the following, we shall analyze the convergence behaviors and stability properties of our practical computation (can be abstractly formulated as Eq. (6)) from the perturbation analysis perspective. Specifically, we consider the errors for solving $\bar{\mathbf{x}}$ as the perturbation of optimizing Eq. (4) and obtain the following constructive results:

4. Please notice that Eq. (6) is only used for our theoretical analysis, but not practical computation.

- Convergence (Theorem 2): As the error δ decreases to 0, the solution of Eq. (6) strictly converges to the solution set of the bilevel problem in Eq. (2).
- Stability (Theorem 3): The proximity from the optimal solution of Eq. (6) to the solution set of bilevel problem in Eq. (2) can be strictly dominated in terms of δ .

4.1 Convergence Analysis

Before proving our formal convergence result, we first introduce some necessary notations. By respectively considering $\mathcal{A}(\bar{\mathbf{x}}_{\delta})$ and $\varphi(\bar{\mathbf{x}}_{\delta})$ in Eq. (6) as perturbed $\bar{\mathbf{y}}$ and $\bar{\mathbf{s}}$, we are now aim to investigate the stability of the following parameterized optimization problem

$$(P_{\mathbf{p}}) \quad \min_{\mathbf{x}} F(\mathbf{x}), \text{ s.t. } \begin{cases} \mathcal{A}(\mathbf{x}) - \bar{\mathbf{y}} = \mathbf{p}_1, \\ \varphi(\mathbf{x}) \leq \bar{\mathbf{s}} + \mathbf{p}_2, \end{cases} \quad (7)$$

where $\mathbf{p} = \{\mathbf{p}_1, \mathbf{p}_2\}$, $\bar{\mathbf{y}} = \mathcal{A}(\bar{\mathbf{x}})$ and $\bar{\mathbf{s}} = \varphi(\bar{\mathbf{x}})$ for any given $\bar{\mathbf{x}} \in \mathcal{X}$. Moreover, we shall need the following notations.

- The feasible set mapping of $P_{\mathbf{p}}$: $\mathcal{S}_{feas}(\mathbf{p}) := \{\mathbf{x} | \mathcal{A}(\mathbf{x}) - \bar{\mathbf{y}} = \mathbf{p}_1, \varphi(\mathbf{x}) \leq \bar{\mathbf{s}} + \mathbf{p}_2\}$.
- The optimal value mapping of $P_{\mathbf{p}}$: $\mathcal{S}_{val}(\mathbf{p}) := \inf_{\mathbf{x}} \{F(\mathbf{x}) | \mathcal{A}(\mathbf{x}) - \bar{\mathbf{y}} = \mathbf{p}_1, \varphi(\mathbf{x}) \leq \bar{\mathbf{s}} + \mathbf{p}_2\}$.
- The solution set mapping of $P_{\mathbf{p}}$: $\mathcal{S}_{sol}(\mathbf{p}) := \{\mathbf{x} \in \mathcal{S}_{feas}(\mathbf{p}) | F(\mathbf{x}) = \mathcal{S}_{val}(\mathbf{p})\}$.

Continuity properties of set-valued mapping $\mathcal{S} : \mathbb{R}^m \rightrightarrows \mathbb{R}^n$ is developed in terms of outer and inner limits:

$$\begin{aligned} \limsup_{\mathbf{p} \rightarrow \bar{\mathbf{p}}} \mathcal{S}(\mathbf{p}) &:= \{\mathbf{x} | \exists \mathbf{p}^v \rightarrow \bar{\mathbf{p}}, \exists \mathbf{x}^v \rightarrow \mathbf{x} \text{ with } \mathbf{x}^v \in \mathcal{S}(\mathbf{p}^v)\}, \\ \liminf_{\mathbf{p} \rightarrow \bar{\mathbf{p}}} \mathcal{S}(\mathbf{p}) &:= \{\mathbf{x} | \forall \mathbf{p}^v \rightarrow \bar{\mathbf{p}}, \exists \mathbf{x}^v \rightarrow \mathbf{x} \text{ with } \mathbf{x}^v \in \mathcal{S}(\mathbf{p}^v)\}. \end{aligned}$$

Definition 1. *A set-valued mapping $\mathcal{S} : \mathbb{R}^m \rightrightarrows \mathbb{R}^n$ is outer semicontinuous (OSC) at $\bar{\mathbf{p}}$ when $\limsup_{\mathbf{p} \rightarrow \bar{\mathbf{p}}} \mathcal{S}(\mathbf{p}) \subseteq \mathcal{S}(\bar{\mathbf{p}})$ and inner semicontinuous (ISC) at $\bar{\mathbf{p}}$ when $\liminf_{\mathbf{p} \rightarrow \bar{\mathbf{p}}} \mathcal{S}(\mathbf{p}) \supseteq \mathcal{S}(\bar{\mathbf{p}})$. It is called continuous at $\bar{\mathbf{p}}$ when it is both OSC and ISC at $\bar{\mathbf{p}}$, as expressed by $\lim_{\mathbf{p} \rightarrow \bar{\mathbf{p}}} \mathcal{S}(\mathbf{p}) = \mathcal{S}(\bar{\mathbf{p}})$.*

Lemma 1. *Suppose that F is a continuous function. If $\mathcal{S}_{feas}(\mathbf{p})$ is continuous at 0 and $\mathcal{S}_{sol}(0) \neq \emptyset$, then $\mathcal{S}_{sol}(\mathbf{p})$ is outer semicontinuous at 0.*

Remark 2. *We shall clarify the continuity assumption regarding \mathcal{S}_{feas} in Lemma 1. In fact, when φ is a convex polyhedral function, \mathcal{S}_{feas} is a closed polyhedral convex mapping. Then according to Theorem 3C.3 in [32], we know that \mathcal{S}_{feas} is Lipschitz continuous, i.e. there exists $\kappa \geq 0$ such that for all $\mathbf{p}_1, \mathbf{p}_2 \in \text{dom} \mathcal{S}_{feas}$,*

$$h(\mathcal{S}_{feas}(\mathbf{p}_1), \mathcal{S}_{feas}(\mathbf{p}_2)) \leq \kappa \|\mathbf{p}_1 - \mathbf{p}_2\|,$$

where for any nonempty sets \mathcal{E} and \mathcal{F} , $h(\mathcal{E}, \mathcal{F})$ is given by $h(\mathcal{E}, \mathcal{F}) = \max\{e(\mathcal{E}, \mathcal{F}), e(\mathcal{F}, \mathcal{E})\}$, and $e(\mathcal{E}, \mathcal{F}) = \sup_{\mathbf{x} \in \mathcal{E}} d(\mathbf{x}, \mathcal{F})$. Therefore, when φ is a convex polyhedral function, all the assumptions about \mathcal{S}_{feas} in the lemma above are satisfied.

Now we are ready to induce the main result to guarantee the convergence of our proposed optimization scheme.

Theorem 2. *Suppose that φ is a convex polyhedral function and let $\{\mathbf{x}_{\delta_k}^*\}$ be the solution returned by solving Eq. (6) with errors $\{\delta_k\}$. If $\delta_k \rightarrow 0$, then*

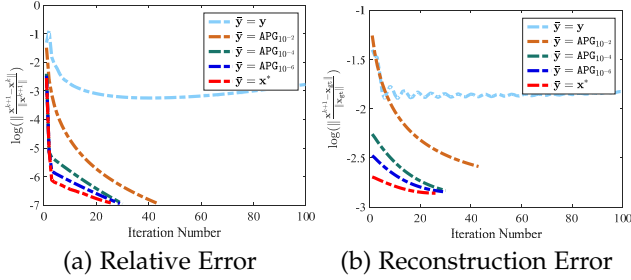

 Fig. 1. The iteration behaviors of BIO with different \bar{y} .

TABLE 1

Quantitative results of BIO with different settings in Figs. 1-2. Time_1 and Time_2 are the CPU time (in seconds) for calculating \bar{y} and the iteration of BIO, respectively.

\mathcal{D}	\bar{y}	Time_1	Time_2	PSNR	SSIM
Deconv	\mathbf{x}_{gt}	—	0.5430	51.33	0.9988
	\mathbf{y}	—	2.9989	25.37	0.6720
	$\text{APG}_{10^{-2}}$	0.1478	1.2901	26.62	0.7797
	$\text{APG}_{10^{-4}}$	1.7843	0.9153	34.82	0.9662
	$\text{APG}_{10^{-6}}$	70.6342	0.8953	34.93	0.9577
	\mathbf{x}^*	131.0989	0.8339	34.96	0.9400
\mathcal{I}		1.7843	2.1665	29.63	0.9029
CNN	$\text{APG}_{10^{-4}}$	1.7843	0.3729	36.18	0.9728

- 1) For any accumulation point \mathbf{x}^* of the sequence $\{\mathbf{x}_{\delta_k}^*\}$, we have that $\mathbf{x}^* \in \mathcal{S}_{\text{sol}}(0)$. That is, \mathbf{x}^* solves bilevel problem Eq. (2).
- 2) If F is coercive, then the sequence $\{\mathbf{x}_{\delta_k}^*\}$ is bounded and hence admits at least one accumulation point.

4.2 Stability Analysis

Before we can establish the desired stability result for Eq. (6), we need the following general stability analysis as preliminaries.

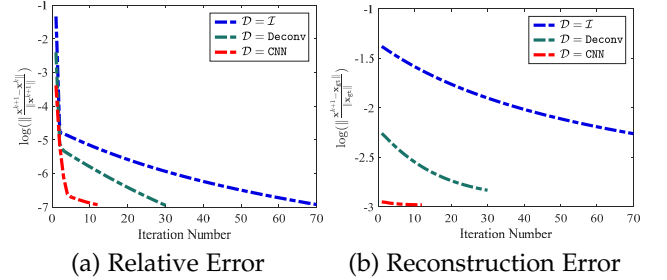
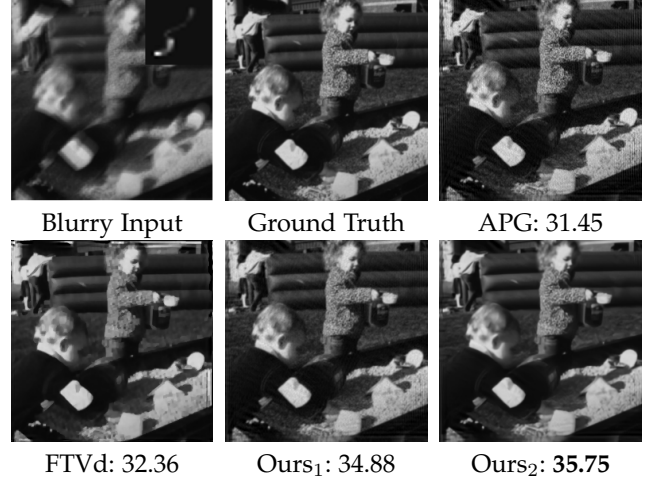
Proposition 1. Suppose that there exists neighborhood \mathcal{N} of some point $\bar{\mathbf{x}} \in \mathcal{S}_{\text{sol}}(0)$ such that $F(\mathbf{x}) \geq F(\bar{\mathbf{x}}) + \frac{\epsilon}{2}d(\mathbf{x}, \mathcal{S}_{\text{sol}}(0))^2$, $\forall \mathbf{x} \in \mathcal{N} \cap \mathcal{S}_{\text{feas}}(0)$, where F is Lipschitz continuous with modulus L on \mathcal{N} , and there exist κ_1, κ_2 such that $\mathcal{S}_{\text{feas}}(\mathbf{p}) \cap \mathcal{N} \subseteq \mathcal{S}_{\text{feas}}(0) + \kappa_1 \|\mathbf{p}\| \mathbb{B}$, and $\mathcal{S}_{\text{feas}}(0) \cap \mathcal{N} \subseteq \mathcal{S}_{\text{feas}}(\mathbf{p}) + \kappa_2 \|\mathbf{p}\| \mathbb{B}$. Then for any $\mathbf{x}_p \in \mathcal{S}_{\text{sol}}(\mathbf{p}) \cap \mathcal{N}$, we have $d(\mathbf{x}_p, \mathcal{S}_{\text{sol}}(0)) \leq \kappa_1 \|\mathbf{p}\| + \left(\frac{(\kappa_1 + \kappa_2)L}{c}\right)^{\frac{1}{2}} \|\mathbf{p}\|^{\frac{1}{2}}$.

According to the results obtained above, together with the arguments given in the proof of Theorem 2, we also have following stability guarantees as follows.

Theorem 3. For given $\delta > 0$, let \mathbf{x}_{δ}^* represents the solution returned by solving Eq. (6). Suppose that φ is a convex polyhedral function. If there exists a neighborhood \mathcal{N} of some point $\bar{\mathbf{x}} \in \mathcal{S}_{\text{sol}}(0)$ such that $F(\mathbf{x}) \geq F(\bar{\mathbf{x}}) + \frac{\epsilon}{2}d(\mathbf{x}, \mathcal{S}_{\text{opt}}(0))^2$, $\forall \mathbf{x} \in \mathcal{N} \cap \mathcal{S}_{\text{feas}}(0)$, and F is Lipschitz continuous on \mathcal{N} , then there exist $c_1, c_2 > 0$ such that for any $\mathbf{x}_{\delta}^* \in \mathcal{N}$, we have $d(\mathbf{x}_{\delta}^*, \mathcal{S}_{\text{sol}}(0)) \leq c_1 \delta + c_2 \delta^{1/2}$.

5 BIO FOR IIPs IN COMPUTER VISION

Indeed, a variety of computer vision tasks can be considered as IIPs. So in this section we demonstrate how to apply BIO


 Fig. 2. The iteration behaviors of BIO with different \mathcal{D} .

 Fig. 3. Comparisons of APG, FTVd, Ours₁ (BIO with Deconv) and Ours₂ (BIO with CNN). The PSNR score is reported below each subfigure.

to formulate and optimize typical computer vision problems (e.g., image restoration and compressive sensing MRI)⁵.

Specifying Knowledge-driven Latent Feasibility. In particular, we first specify the lower-level subproblem by defining $\psi(\mathbf{x}) = \|\mathcal{A}(\mathbf{x}) - \mathbf{y}\|^2$ and $\varphi(\mathbf{x}) = \gamma \|\nabla \mathbf{x}\|_1$ in Eq. (2) to reveal the task information (i.e., fidelity) and the natural image distributions (i.e., priors), respectively. Here $\|\nabla \mathbf{x}\|_1$ denotes the ℓ_1 norm on the image gradient (a.k.a. total variation regularization [3]), which has been recognized as a proper and generic distribution assumption for the natural images. As for the task-specific fidelity, $\psi(\mathbf{x})$ is actually used to guarantee that \mathbf{x} should be structurally similar to the observation \mathbf{y} after the degradation \mathcal{A} . So we define \mathcal{A} as a blur matrix \mathbf{K} for image restoration [5] or under-sampling matrix \mathbf{P} and Fourier transformation \mathbf{F} for compressive sensing MRI (i.e., $\mathcal{A}(\mathbf{x}) = \mathbf{P}\mathbf{F}\mathbf{x}$) [27]. In this way, we actually define a nested optimization task to introduce implicit feasibility to narrow down the solution space. We argue that compared with these explicitly defined constraints in standard optimization model, which can only reveal straightforward conditions, the knowledge-driven latent feasibility provided by BIO is definitely more flexible and powerful.

Investigating Data-driven Loss Function. With the given latent constraints, we are ready to introduce our upper-level subproblem in Eq. (2). Indeed, we only slightly modify the standard loss function as $f(\mathbf{x}) = \|\mathbf{x} - \mathcal{D}(\mathbf{y})\|^2$,

⁵ Please refer to Appendix for more algorithmic details of these applications.

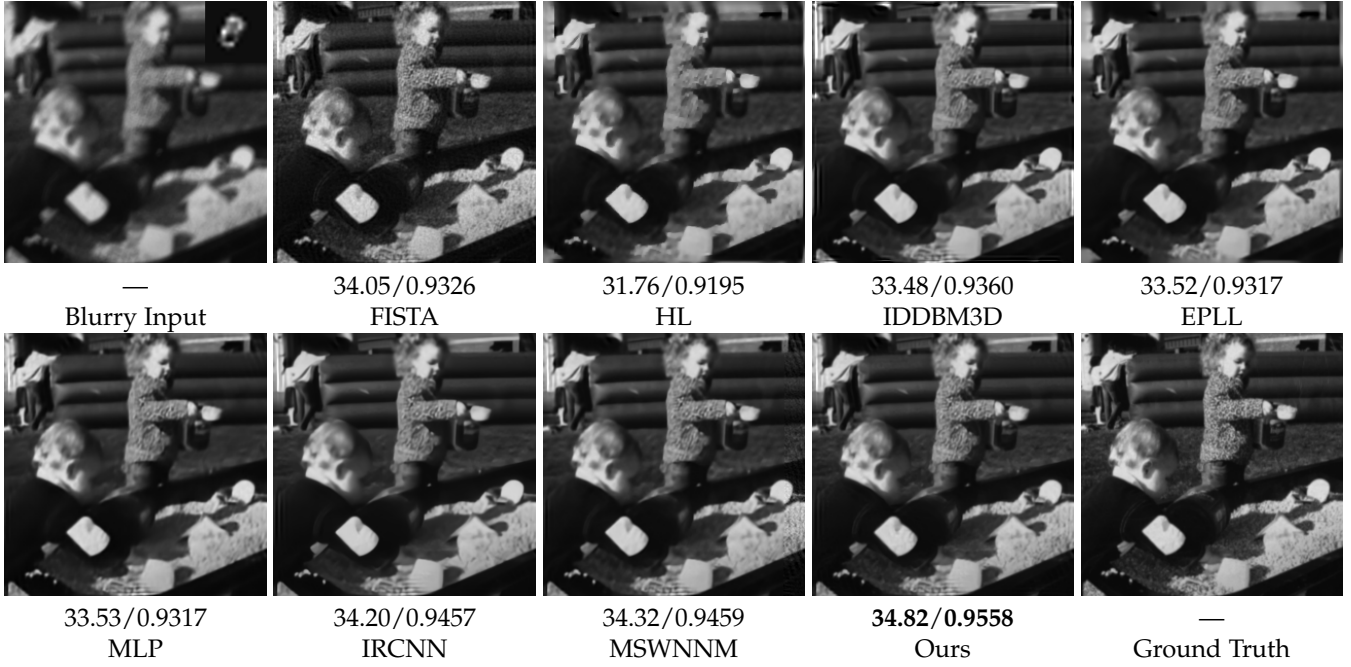


Fig. 4. Results of images corrupted by a kernel with the size of 15×15 from Levin et al' dataset [34]. The PSNR/SSIM scores are reported below each subfigure.

where \mathcal{D} denotes a given mapping (e.g., pre-trained deep network architectures) on the observed image. Thus by learning \mathcal{D} on collected training set, we can successfully incorporate data information in BIO formulation⁶. Furthermore, thanks to the generic structure in Eq. (2), we can also introduce additional priors using g to enforce specific constraints on \mathbf{x} . For example, in CS-MRI problem, we introduce a nonsmooth regularization $g(\mathbf{x}) = \rho \|\mathbf{T}\mathbf{x}\|_1$ with a transform \mathbf{T} (e.g., Discrete Cosine Transform (DCT) or Discrete Wavelet Transform (DWT), etc) to further induce sparsity of images in the transformed space [33].

6 EXPERIMENTAL RESULTS

In this section, we first conduct numerical experiments to study the iteration and convergence behaviors of our proposed BIO. Then we compare the practical performance of BIO with state-of-the-art approaches (including deep learning methods) on two real-world IIP applications in low-level computer vision area, i.e., image restoration and compressed sensing MRI. All the experiments are conducted on a PC with Intel Core i7 CPU at 3.7GHz, 32GB RAM and a NVIDIA GeForce GTX 1080Ti 11GB GPU.

6.1 Model Evaluation and Verification

We first analyze and evaluate the important components of BIO on the image restoration task. As discussed in the above theoretical part, it is necessary to specify a particular $\bar{\mathbf{y}}$ to setup our algorithm. Here we consider different strategies to obtain it, i.e., set $\bar{\mathbf{y}}$ as the corrupted observation \mathbf{y} , or the numerical solutions i.e., $\bar{\mathbf{y}} = \mathcal{A}(\mathbf{x}_{\text{APG}})$, where \mathbf{x}_{APG} is returned by solving the lower-level subproblem in Eq. (1) by APG [35] with different relative errors (i.e., $\|\mathbf{x}^{k+1} - \mathbf{x}^k\| / \|\mathbf{x}^{k+1}\|$ is less

than 10^{-2} , 10^{-4} or 10^{-6}). These three settings are denoted as $\text{APG}_{10^{-2}}$, $\text{APG}_{10^{-4}}$ and $\text{APG}_{10^{-6}}$ in Table 1 and Fig. 1. We also consider the optimal solution of the lower-level subproblem (i.e., $\bar{\mathbf{y}}^* = \mathcal{A}(\mathbf{x}^*)$)⁷ in these experiments as a reference. It can be seen from Fig. 1 and Table 1 (the top part) that the performance of BIO with $\bar{\mathbf{y}}^*$ is the upper bound of all these settings. We also observed that both $\text{APG}_{10^{-4}}$ and $\text{APG}_{10^{-6}}$ obtain very close results to the ideal $\bar{\mathbf{y}}^*$ strategy. But the speed of $\text{APG}_{10^{-4}}$ is much higher than $\text{APG}_{10^{-6}}$. All these results actually have verified the nice convergence and stability properties of BIO. Thus in the following we always adopt $\text{APG}_{10^{-4}}$ to setup BIO for these applications.

It is known that another important component of BIO is the operator \mathcal{D} in the upper-level subproblem. Here we also consider different strategies to design \mathcal{D} . Specifically, the most naive way to obtain this operator is just setting it as the identity mapping (i.e., $\mathcal{D}(\mathbf{y}) = \mathbf{y}$, denoted as \mathcal{I}). We can also define this operator by introducing a deconvolution loss and solving it in closed-form (denoted as Deconv), i.e., $\mathcal{D}(\mathbf{y}) = \arg \min_{\mathbf{x}} \|\mathbf{K}\mathbf{x} - \mathbf{y}\|^2 + \alpha \|\mathbf{x} - \mathbf{y}\|^2$ with a trade-off $\alpha > 0$ (fix it as 10^{-4} for all the experiments). Inspired by the recent developments of deep learning, here we also introduce convolution neural networks (CNN) [36] as \mathcal{D} (denoted as CNN) in BIO. That is, we design a simple denoising CNN architecture, which consists of seven dilated convolutions, six ReLU operations (plugged between each two convolution layers), and five batch normalizations (plugged between convolution and ReLU, except the first convolution layer). We collected 800 natural images from ImageNet database [37] and add 5% Gaussian noises to generate the training data for our CNN-based denoiser in all the experiments. We observed in Fig. 2 and Table 1

⁷ Since the lower-level subproblem in Eq. (1) is convex and APG is also a strictly converged method, here we just compute 20,000 iterations to numerically obtain the optimal solution \mathbf{x}^* .

⁶ We state the details on the design and training of \mathcal{D} in Sec. 6.

TABLE 2
Averaged image restoration quantitative performance (i.e., PSNR and SSIM) on Levin et al.' benchmark.

	FTVd [3]	FISTA [38]	HL [39]	IDDBM3D [40]	EPLL [41]	MLP	IRCNN [11]	MSWNNM [5]	BIO (Ours)
PSNR	29.38	31.81	30.12	31.53	31.65	31.32	32.28	32.50	32.79
SSIM	0.8819	0.9010	0.8961	0.9043	0.9258	0.8991	0.9200	0.9247	0.9318

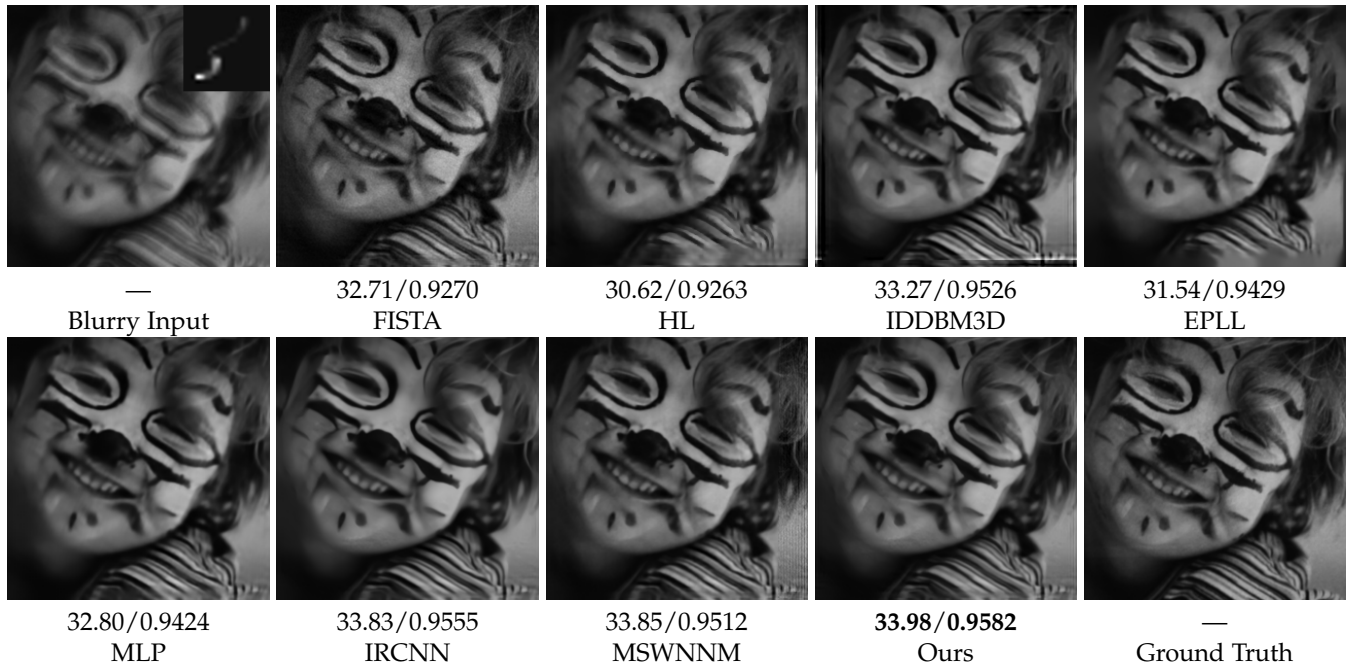


Fig. 5. Results of images corrupted by a kernel with the size of 21×21 from Levin et al.' dataset [34]. The PSNR/SSIM scores are reported below each subfigure.

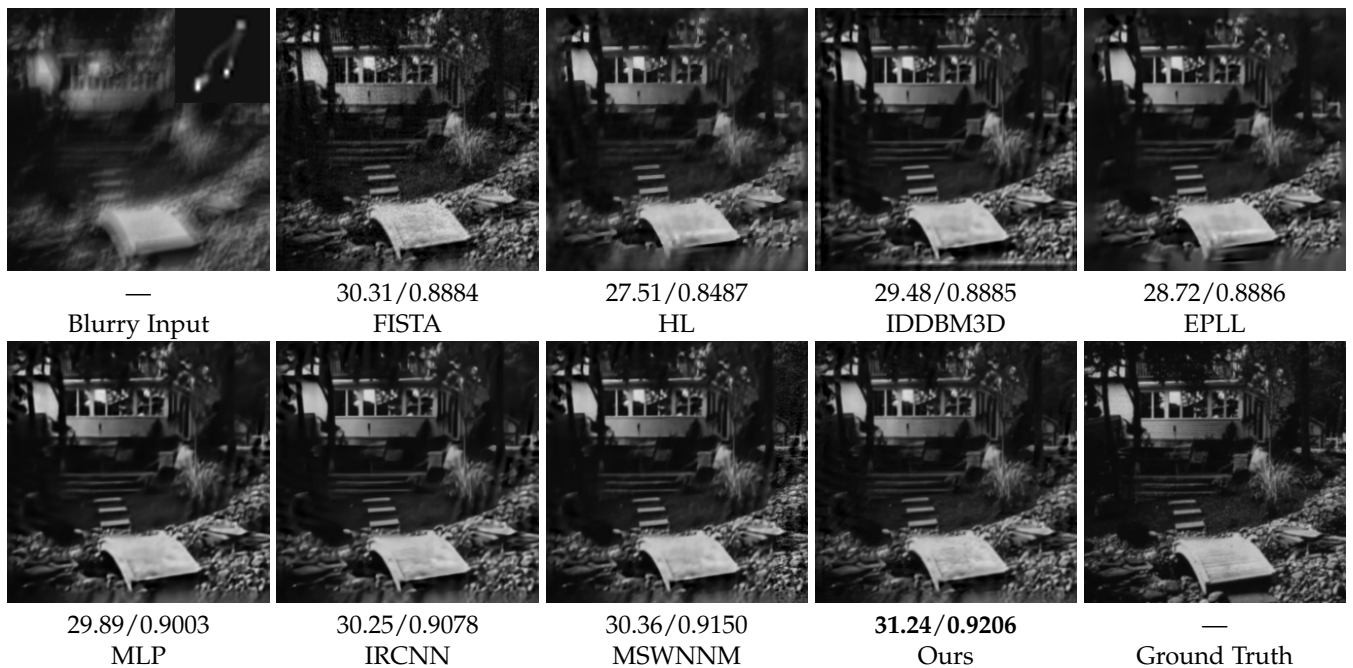


Fig. 6. Results of images corrupted by a kernel with the size of 23×23 from Levin et al.' dataset [34]. The PSNR/SSIM scores are reported below each subfigure.

that the task-inspired Deconv operation is better than the naive \mathcal{I} strategy. While our learning-based CNN module can significantly improve both the numerical performance

and the final quantitative and qualitative results, which successfully verify the values of our knowledge and data integration paradigm in BIO.

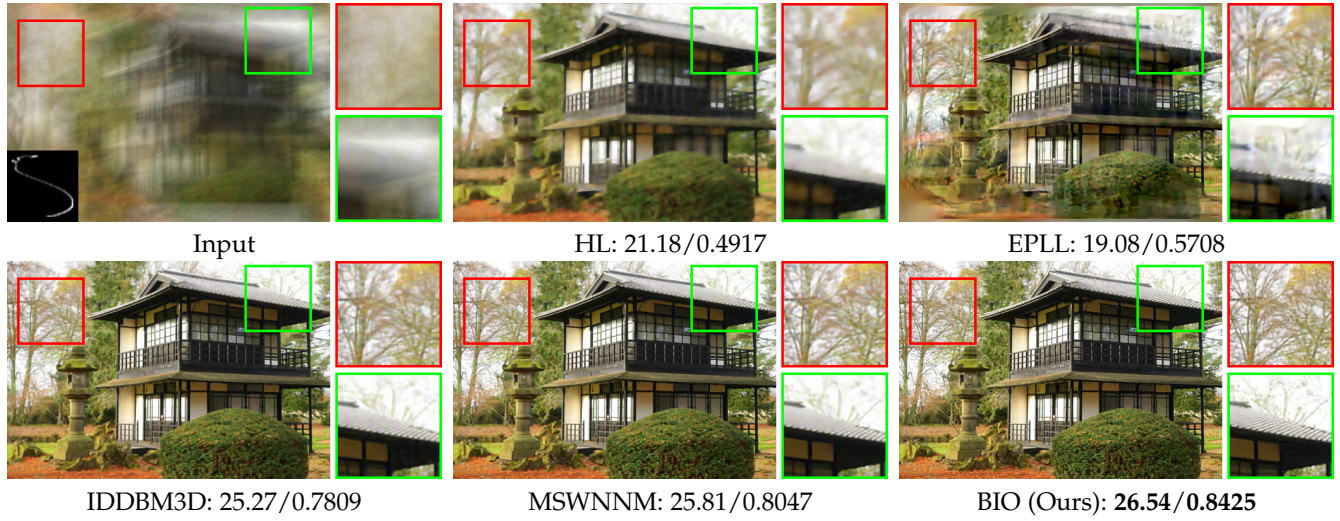


Fig. 7. Image restoration results on a challenging color image with a large-size kernel (75×75). The PSNR/SSIM scores are reported below each subfigure. The PSNR/SSIM scores are reported below each subfigure.

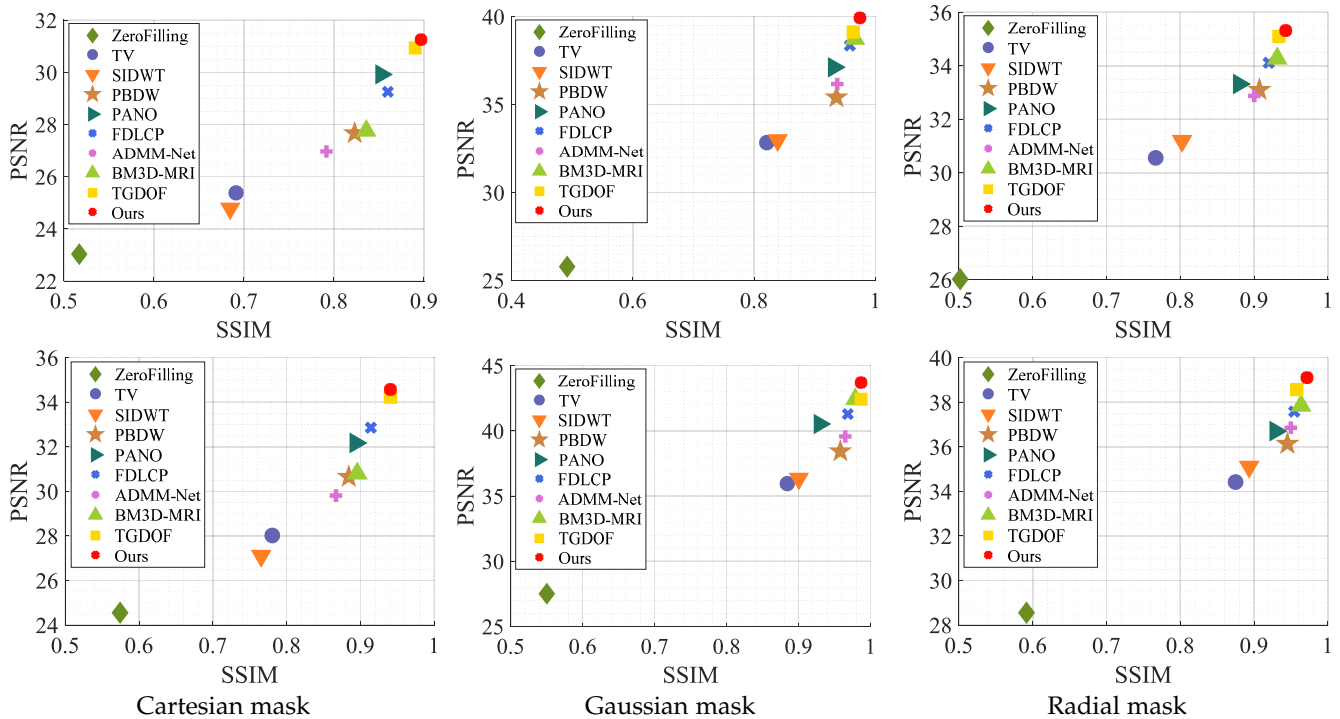


Fig. 8. Averaged compressed sensing MRI results on IXI dataset. Top and Bottom row are 20% and 30% sampling rate, respectively. In each subfigure, the upper right is the best.

From the optimization perspective, we can also understand that BIO actually provides a bilevel way to improve the optimization process of the lower-level model. To verify this effectiveness, we utilize two well-known numerical optimization methods, i.e., FTVd [3] and APG [35], to directly solve the lower-level model in Eq. (1). We compared their results and two versions of our BIO, including Ours₁ (with the Deconv) and Ours₂ (with the CNN) in Fig. 3. It can be easily seen that both of our two BIO solvers obtained remarkably better performance than traditional numerical optimization approaches. Especially, the learning-based CNN strategy is the best among all the compared methods, which successfully verify the power of our data-driven bilevel

integration mechanism.

6.2 Applications in Computer Vision

Image Restoration. We now compare BIO with state-of-the-art image restoration approaches, including FTVd [3], FISTA [38], HL [39], IDDBM3D [40], EPLL [41], MLP [42], IRCNN [11] and MSWNNM [5]. We first conduct experiments on the well-known Levin et al.' benchmark [34], which includes 32 images of the size 255×255 and blurred by 8 different kernels of the size ranging from 13×13 to 27×27 . The visual comparisons on three example images from this benchmark are plotted in Fig. 4-6, it can be easily seen that our proposed algorithm achieves the prominent detail

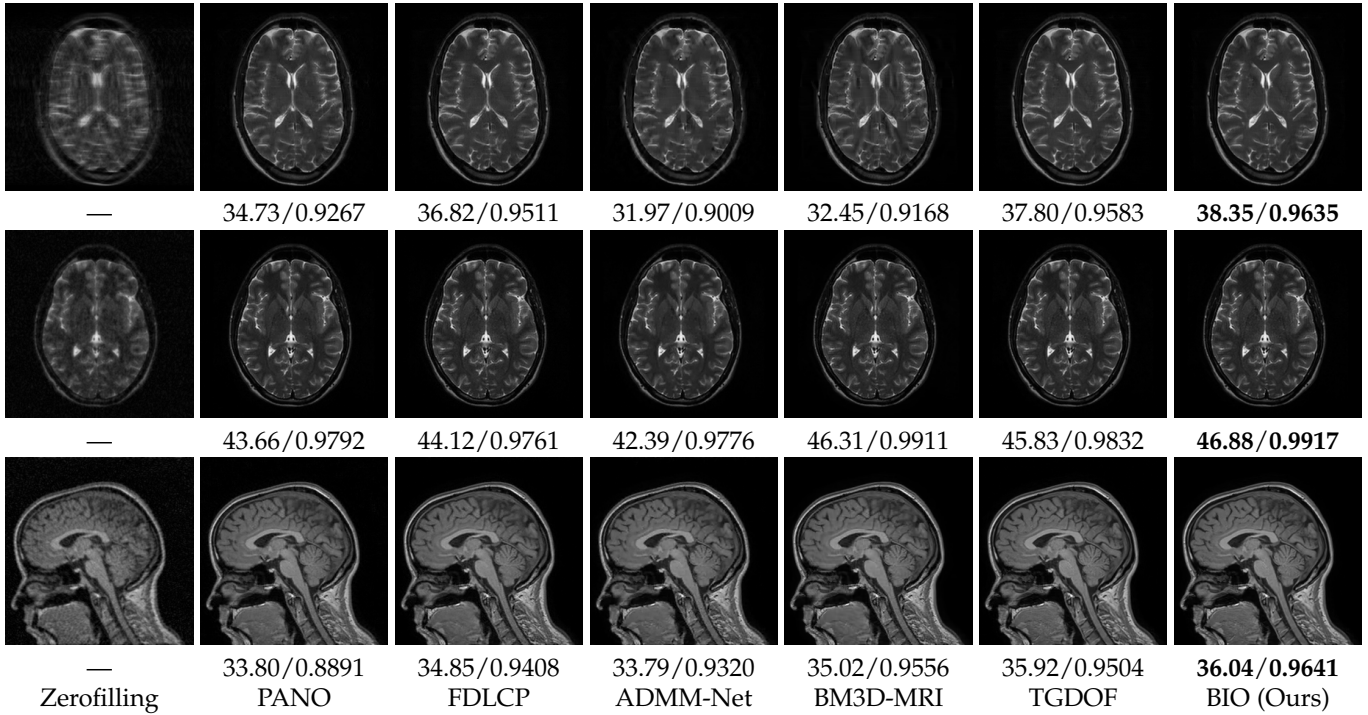


Fig. 9. Visual comparison of Compressive Sensing MRI at the sparse k -space data with different undersampling patterns and 30% sampling rates (Top row: Cartesian mask. Middle row: Gaussian mask. Bottom row: Radial mask).

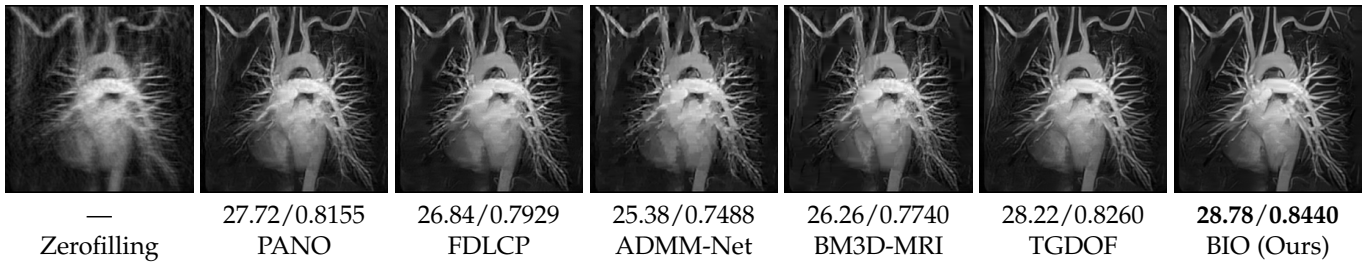


Fig. 10. Visual comparison of Cartesian mask at 30% sampling rate). The PSNR/SSIM scores are reported below each subfigure.

recovery with highest PSNR/SSIM scores in different cases. We also report the averaged quantitative scores (i.e., PSNR and SSIM) in Table 2. We can see that the deep learning based IRCNN approach can achieve much better performance than traditional optimization based methods. The very recently developed MSWNNM adopted a multi-scale technique to investigate rich image details, thus its results are even better. While thanks to the novel interpretation of knowledge-driven and data-driven mechanisms, our BIO obtain the best quantitative and qualitative results among all the tested methods. In addition, a color image (612×342) corrupted by a very large kernel (of the size 75×75) is also utilized to further evaluate these approaches, which is showed in Fig. 7. Obviously, all these compared state-of-the-art approaches tend to the unclear details depict. Again, BIO recovered richer textures and more details of the image, thus performed the best.

Compressive Sensing MRI (CS-MRI). We then evaluate BIO on the CS-MRI problem. Specifically, we conduct all the experiments on 55 images with the size of

256×256 from the widely-used IXI MRI benchmark⁸. Our experiments contains three types of undersampling patterns (i.e., Cartesian, Gaussian, and Radial mask) and two sampling rates (i.e., 20%, 30%) to generate the sparse k -space data. We compared BIO with many existing state-of-the-art methods including TV [43], SIDWT [33], PBDW [44], PANO [45], FDLCP [46], ADMM-Net [27], BM3D-MRI [18], and TGDOF [47]. The scatter plots in Fig. 8 illustrated the quantitative results of all the compared approaches on the test data set, including three types of undersampling patterns and two kinds of sampling rates. It is easy to see that our BIO achieved the best results according to both PSNR and SSIM scores (i.e., the upper right red points) in all situations. We then consider three types of masks with 30% sampling rates to fully verify the performance. All these results are demonstrated in Fig. 9. Clearly, our BIO achieved outstanding performances with richer details and the highest quantitative scores in all these scenarios. Further, we generate challenging chest data using a Cartesian mask with a sampling rate of 30% in Fig. 10. Consistently, BIO

8. <http://brain-development.org/ixi-dataset/>

achieves the best qualitative and quantitative performance. The above sufficient experiments fully indicate the superiority of our BIO in terms of CS-MRI problem.

7 CONCLUSIONS

This paper studied a bilevel optimization paradigm to integrate knowledge and data for formalizing and optimizing ill-posed inverse problems. We theoretically proved our established solving scheme can strictly converge to the global optimal solution of BIO. Plenty of experiments on two real-world computer vision applications fully revealed the efficiency and effectiveness of the proposed framework.

APPENDIX A

PROOFS OF OUR THEORETICAL RESULTS

In the following, we first provide detailed proofs for the propositions and theorems in our manuscript. The details for the bilevel optimization model and iteration schemes for particular applications are also summarized.

A.1 Proof of Theorem 1

Proof. Given a solution $\bar{\mathbf{x}} \in \mathcal{X}$. First, for any $\mathbf{x} \in \{\mathbf{x} | \mathcal{A}(\mathbf{x}) = \mathcal{A}(\bar{\mathbf{x}}), \varphi(\mathbf{x}) \leq \varphi(\bar{\mathbf{x}})\}$, we have $\Psi(\mathbf{x}) = h(\mathcal{A}(\bar{\mathbf{x}})) + \varphi(\mathbf{x}) \leq h(\mathcal{A}(\bar{\mathbf{x}})) + \varphi(\bar{\mathbf{x}}) = \min_{\mathbf{x}} \Psi(\mathbf{x})$, thus

$$\{\mathbf{x} | \mathcal{A}(\mathbf{x}) = \mathcal{A}(\bar{\mathbf{x}}), \varphi(\mathbf{x}) \leq \varphi(\bar{\mathbf{x}})\} \subseteq \mathcal{X}. \quad (8)$$

For any $\mathbf{x} \in \mathcal{X}$, if $\mathcal{A}(\mathbf{x}) \neq \mathcal{A}(\bar{\mathbf{x}})$, then by the strong convexity of h , there exists $\sigma > 0$ such that

$$h(\mathcal{A}(\mathbf{x})) \geq h(\mathcal{A}(\bar{\mathbf{x}})) + \langle \nabla h(\mathcal{A}(\bar{\mathbf{x}})), \mathcal{A}(\mathbf{x}) - \mathcal{A}(\bar{\mathbf{x}}) \rangle + \frac{\sigma}{2} \|\mathcal{A}(\mathbf{x}) - \mathcal{A}(\bar{\mathbf{x}})\|^2.$$

And since $0 \in \mathcal{A}^T \nabla h(\mathcal{A}(\bar{\mathbf{x}})) + \partial \varphi(\bar{\mathbf{x}})$, by the convexity of g , we have

$$\varphi(\mathbf{x}) \geq \varphi(\bar{\mathbf{x}}) + \langle -\mathcal{A}^T \nabla h(\mathcal{A}(\bar{\mathbf{x}})), \mathbf{x} - \bar{\mathbf{x}} \rangle.$$

Combining the two inequalities given above, we obtain

$$\Psi(\mathbf{x}) \geq \Psi(\bar{\mathbf{x}}) + \frac{\sigma}{2} \|\mathcal{A}(\mathbf{x}) - \mathcal{A}(\bar{\mathbf{x}})\|^2 > \Psi(\bar{\mathbf{x}}),$$

which contradicts to the fact that $\mathbf{x} \in \mathcal{X}$. Next, since $\mathcal{A}(\mathbf{x}) = \mathcal{A}(\bar{\mathbf{x}})$, and $\Psi(\mathbf{x}) = \Psi(\bar{\mathbf{x}})$, we have $\varphi(\mathbf{x}) = \varphi(\bar{\mathbf{x}})$, and thus

$$\mathcal{X} \subseteq \{\mathbf{x} | \mathcal{A}(\mathbf{x}) = \mathcal{A}(\bar{\mathbf{x}}), \varphi(\mathbf{x}) \leq \varphi(\bar{\mathbf{x}})\}. \quad (9)$$

Upon combining Eq. (8) and Eq. (9), we reach the re-characterization of \mathcal{X} as Eq. (3). \square

A.2 Proof of Corollary 1

Remark 3. *Indeed, we can further estimate a nice linear convergence rate of Eq. (5) for particular models. That is, if we have that f takes the form that $f(\mathbf{x}) = h(\tilde{\mathcal{A}}\mathbf{x})$ where $\tilde{\mathcal{A}}$ is some given linear operator, h satisfies Assumption 1, g represents (1) convex polyhedral regularizer; (2) group-lasso regularizer; (3) sparse group lasso regularizer, ψ is a convex polyhedral function, then $\{(\mathbf{x}^k, \mathbf{z}^k, \mathbf{s}^k, \boldsymbol{\lambda}^k)\}$ converges linearly to the KKT point set of problem in Eq. (4). In particular, the sequence $\{\mathbf{x}^k\}$ converges linearly to the global optimal solutions of Eq. (2).*

Proof. By Theorem 1, we have the equivalence between Eq. (2) and Eq. (4). Thus the convergence of the iterations in Eq. (5) can be directly guaranteed via standard convergence results of proximal ADMM [48]. Moreover, by applying the investigations in [49], we can further obtain a linear convergence rate estimation for our iteration in Eq. (5). \square

A.3 Proof of Lemma 1

Inspired by Theorem 3B.5 in [32], we have following result.

Proof. First, we show that $\limsup_{\mathbf{p} \rightarrow 0} \mathcal{S}_{val}(\mathbf{p}) \leq \mathcal{S}_{val}(0)$. Let $\bar{\mathbf{x}} \in \mathcal{S}_{sol}(0)$, since $\mathcal{S}_{feas}(\mathbf{p})$ is continuous at 0, it is inner semicontinuous at 0. Thus for any sequence $\mathbf{p}^k \rightarrow 0$, we get the existence of a sequence of points \mathbf{x}^k with $\mathbf{x}^k \in \mathcal{S}_{feas}(\mathbf{p}^k)$ such that $\mathbf{x}^k \rightarrow \bar{\mathbf{x}}$ as $k \rightarrow \infty$. Then for any $\epsilon > 0$ there exists $N > 0$ such that

$$\mathcal{S}_{val}(\mathbf{p}^k) \leq F(\mathbf{x}^k) \leq F(\bar{\mathbf{x}}) + \epsilon = \mathcal{S}_{val}(0) + \epsilon, \quad \forall k \geq N,$$

which implies

$$\limsup_{\mathbf{p} \rightarrow 0} \mathcal{S}_{val}(\mathbf{p}) \leq \mathcal{S}_{val}(0).$$

We next show the outer semicontinuity of \mathcal{S}_{sol} at 0. For any $\mathbf{p}^k \rightarrow 0$ with $\mathbf{x}^k \in \mathcal{S}_{opt}(\mathbf{p}^k)$ such that $\mathbf{x}^k \rightarrow \bar{\mathbf{x}}$. Since \mathcal{S}_{feas} is outer semicontinuous at 0, we have $\bar{\mathbf{x}} \in \mathcal{S}_{feas}(0)$. By the continuity of F and upper semicontinuity of \mathcal{S}_{val} at 0, we have

$$\mathcal{S}_{val}(0) \leq F(\bar{\mathbf{x}}) = \lim_{k \rightarrow \infty} F(\mathbf{x}^k) = \limsup_{k \rightarrow \infty} \mathcal{S}_{val}(\mathbf{p}^k) \leq \mathcal{S}_{val}(0),$$

which implies

$$\bar{\mathbf{x}} \in \mathcal{S}_{sol}(0).$$

That is, $\mathcal{S}_{sol}(\mathbf{p})$ is outer semicontinuous at 0 according to Definition 1. \square

A.4 Proof of Theorem 2

Proof. Because for any \mathbf{x}_{δ}^* , we have $\mathbf{x}_{\delta}^* \in \mathcal{S}_{sol}(\mathbf{p})$ with $\mathbf{p}_1 = \mathcal{A}(\bar{\mathbf{x}}_{\delta}) - \mathcal{A}(\bar{\mathbf{x}})$ and $\mathbf{p}_2 = \varphi(\bar{\mathbf{x}}_{\delta}) - \varphi(\bar{\mathbf{x}})$. Therefore, $\|\mathbf{p}\| \leq \|\mathcal{A}(\bar{\mathbf{x}}_{\delta}) - \mathcal{A}(\bar{\mathbf{x}})\| + \|\varphi(\bar{\mathbf{x}}_{\delta}) - \varphi(\bar{\mathbf{x}})\| \leq (\|\mathcal{A}\| + L_{\varphi})d(\bar{\mathbf{x}}_{\delta}, \mathcal{X}) \leq (\|\mathcal{A}\| + L_{\varphi})\delta$, where L_{φ} is the Lipschitz continuity modulus of φ . Note that the Lipschitz continuity modulus is guaranteed to exist because φ is a convex polyhedral function. Then the first argument follows from Lemma 1 directly. The second argument actually follows from the fact that $\limsup_{k \rightarrow \infty} F(\mathbf{x}_{\delta_k}^*) \leq \mathcal{S}_{val}(0)$ and F is coercive. \square

A.5 Proof of Proposition 1

Inspired by Proposition 4.37 in [50], we have following result.

Proof. For any $\mathbf{x}_p \in \mathcal{S}_{opt}(\mathbf{p}) \cap \mathcal{N}$, let $\mathbf{z} := \text{Proj}_{\mathcal{S}_{feas}(0)}(\mathbf{x}_p)$ and $\mathbf{x}_0 = \text{Proj}_{\mathcal{S}_{sol}(0)}(\mathbf{z})$, and since $\mathcal{S}_{feas}(0)$ and $\mathcal{S}_{sol}(0)$ are both closed convex sets, \mathbf{z} and \mathbf{x}_0 are well defined. Because $\bar{\mathbf{x}} \in \mathcal{S}_{sol}(0)$, we have $\|\mathbf{x}_0 - \bar{\mathbf{x}}\| \leq \|\mathbf{z} - \bar{\mathbf{x}}\| \leq \|\mathbf{x}_p - \bar{\mathbf{x}}\|$, and thus $\mathbf{z}, \mathbf{x}_0 \in \mathcal{N}$ and $\|\mathbf{x}_p - \mathbf{z}\| \leq \kappa_1 \|\mathbf{p}\|$.

Since $\mathbf{x}_p \in \mathcal{S}_{sol}(\mathbf{p})$, for any point $\mathbf{y} \in \mathcal{S}_{feas}(\mathbf{p})$, we have

$$F(\mathbf{x}_p) - F(\mathbf{x}_0) = F(\mathbf{x}_p) - F(\mathbf{y}) + F(\mathbf{y}) - F(\mathbf{x}_0) \leq L\|\mathbf{y} - \mathbf{x}_0\|.$$

Since \mathbf{y} can be any point in $\mathcal{S}_{feas}(\mathbf{p})$, we have

$$F(\mathbf{x}_p) - F(\mathbf{x}_0) \leq \kappa_2 L \|\mathbf{p}\|. \quad (10)$$

Next, we have

$$\begin{aligned} F(\mathbf{x}_p) - F(\mathbf{x}_0) &\geq F(\mathbf{z}) - F(\mathbf{x}_0) - |F(\mathbf{x}_p) - F(\mathbf{z})| \\ &\geq c\|\mathbf{z} - \mathbf{x}_0\|^2 - L\|\mathbf{x}_p - \mathbf{z}\| \\ &\geq c(\|\mathbf{x}_p - \mathbf{x}_0\| - \|\mathbf{z} - \mathbf{x}_p\|)^2 - \kappa_1 L \|\mathbf{p}\| \\ &\geq c(\|\mathbf{x}_p - \mathbf{x}_0\| - \kappa_1 \|\mathbf{p}\|)^2 - \kappa_1 L \|\mathbf{p}\|. \end{aligned}$$

Combining with Eq. (10), we get

$$\kappa_2 L \|\mathbf{p}\| \geq c(\|\mathbf{x}_p - \mathbf{x}_0\| - \kappa_1 \|\mathbf{p}\|)^2 - \kappa_1 L \|\mathbf{p}\|,$$

and thus

$$d(\mathbf{x}_p, \mathcal{S}_{sol}(0)) \leq \|\mathbf{x}_p - \mathbf{x}_0\| \leq \kappa_1 \|\mathbf{p}\| + \sqrt{\frac{(\kappa_1 + \kappa_2)L}{c} \|\mathbf{p}\|}.$$

□

A.6 Proof of Theorem 3

Proof. As stated in our manuscript, according to the results proved in Proposition 1, together with the arguments given in the proof of Theorem 2, we can directly have the stability guarantees in this theorem. □

APPENDIX B

SPECIFIC ITERATION SCHEMES FOR APPLICATIONS

In this part, the details for the bilevel optimization model and iteration schemes for particular applications including image restoration and CS-MRI are summarized.

B.1 Image Restoration

We specific the general BIO model in Eq. (2) for image restoration as follows:

$$\begin{aligned} \min_{\mathbf{x}} \frac{1}{2} \|\mathbf{x} - \mathcal{D}(\mathbf{y})\|^2, \\ \text{s.t. } \mathbf{x} \in \arg \min_{\mathbf{x}} \frac{1}{2} \|\mathbf{K}\mathbf{x} - \mathbf{y}\|^2 + \gamma \|\nabla \mathbf{x}\|_1, \end{aligned} \quad (11)$$

where \mathbf{y} is the corrupted observation, \mathbf{x} is the desired clean image, \mathbf{K} is a blur matrix, and \mathcal{D} is the data-driven operator. As in the case where the regularizer ψ in Eq. (4) is polyhedral convex, Eq. (4) can be reformulated in the following particular way with auxiliary variables to ease the computation. By introducing auxiliary variables $\mathbf{s}_1, \mathbf{s}_2, r, \mathbf{w}$, we can obtain the feasible set as $\mathcal{X} = \{\mathbf{x} | \mathbf{K}\mathbf{x} = \bar{\mathbf{y}}, \nabla \mathbf{x} + \mathbf{s}_1 - \mathbf{w} = 0, \nabla \mathbf{x} - \mathbf{s}_2 + \mathbf{w} = 0, \langle \mathbf{e}, \mathbf{w} \rangle + r - \bar{t} = 0, \mathbf{s}_1, \mathbf{s}_2, r \geq 0\}$, where $\bar{\mathbf{y}} = \mathbf{K}\bar{\mathbf{x}}$ and $\bar{t} = \gamma \|\nabla \bar{\mathbf{x}}\|_1$ for any given $\bar{\mathbf{x}} \in \mathcal{X}$, \mathbf{e} denotes the all one vector, $\lambda_{\mathbf{x}}, \lambda_{\mathbf{s}_1}, \lambda_{\mathbf{s}_2}, \lambda_r$ are the corresponding dual multipliers. Based on this reformulation, the proximal ADMM updating can be summarized as:

$$\begin{cases} [\mathbf{s}_1^{k+1}]_i = \max \left\{ 0, \frac{\beta([\mathbf{w}^k]_i - [\nabla \mathbf{x}^k]_i) - [\lambda_{\mathbf{s}_1}^k]_i + \tau[\mathbf{s}_1^k]_i}{\beta + \tau} \right\}, \\ [\mathbf{s}_2^{k+1}]_i = \max \left\{ 0, \frac{\beta([\mathbf{w}^k]_i + [\nabla \mathbf{x}^k]_i) + [\lambda_{\mathbf{s}_2}^k]_i + \tau[\mathbf{s}_2^k]_i}{\beta + \tau} \right\}, \\ r^{k+1} = \max \left\{ 0, \frac{\beta(\bar{t} - \langle \mathbf{e}, \mathbf{w}^k \rangle) - \lambda_r^k + \tau r^k}{\beta + \tau} \right\}, \\ \mathbf{w}^{k+1} = ((2\beta + \tau)\mathbf{I} + \beta \mathbf{e}\mathbf{e}^\top)^{-1} \mathbf{c}^k, \\ \mathbf{x}^{k+1} = (\beta \mathbf{K}^\top \mathbf{K} + (1 + \tau)\mathbf{I} + 2\beta \nabla^\top \nabla)^{-1} \mathbf{d}^k, \\ \lambda_{\mathbf{x}}^{k+1} = \lambda_{\mathbf{x}}^k + \beta(\mathbf{K}\mathbf{x}^{k+1} - \bar{\mathbf{y}}), \\ \lambda_{\mathbf{s}_1}^{k+1} = \lambda_{\mathbf{s}_1}^k + \beta(\nabla \mathbf{x}^{k+1} + \mathbf{s}_1^{k+1} - \mathbf{w}^{k+1}), \\ \lambda_{\mathbf{s}_2}^{k+1} = \lambda_{\mathbf{s}_2}^k + \beta(\nabla \mathbf{x}^{k+1} - \mathbf{s}_2^{k+1} + \mathbf{w}^{k+1}), \\ \lambda_r^{k+1} = \lambda_r^k + \beta(\langle \mathbf{e}, \mathbf{w}^{k+1} \rangle + r^{k+1} - \bar{t}), \end{cases}$$

where $\beta, \tau > 0$ are respectively the penalty and regularization parameters, $[\cdot]_i$ denotes the i -th element of the given vector, \mathbf{I} is the identity matrix, and $\mathbf{c}^k = \beta \mathbf{s}_1^{k+1} + \lambda_{\mathbf{s}_1}^k + \beta \mathbf{s}_2^{k+1} - \lambda_{\mathbf{s}_2}^k + (\beta \bar{t} - \beta r^{k+1} - \lambda_r^k) \mathbf{e} + \tau \mathbf{w}^k$, $\mathbf{d}^k = \mathcal{D}(\mathbf{y}) + \beta \mathbf{K}^\top \bar{\mathbf{y}} + \nabla^\top (\beta(\mathbf{s}_2^{k+1} - \lambda_{\mathbf{s}_2}^k) - \beta(\mathbf{s}_1^{k+1} + \lambda_{\mathbf{s}_1}^k)) - \mathbf{K}^\top \lambda_{\mathbf{x}}^k + \tau \mathbf{x}^k$.

B.2 CS-MRI

We specific the general BIO model in Eq. (2) for CS-MRI as follows:

$$\begin{aligned} \min_{\mathbf{x}} \frac{\eta}{2} \|\mathbf{x} - \mathcal{D}(\mathbf{y})\|^2 + \rho \|\mathbf{T}\mathbf{x}\|_1, \\ \text{s.t. } \mathbf{x} \in \arg \min_{\mathbf{x}} \frac{1}{2} \|\mathbf{P}\mathbf{F}\mathbf{x} - \mathbf{y}\|^2 + \gamma \|\nabla \mathbf{x}\|_1, \end{aligned} \quad (12)$$

where \mathbf{x} is the discretized image to be reconstructed, \mathbf{y} is the acquired k -space data, \mathbf{P} is the under-sampling matrix, \mathbf{F} denotes the Fourier transform, \mathbf{T} is also a given transform (e.g., Discrete Cosine Transform (DCT) or Discrete Wavelet Transform (DWT), etc) and \mathcal{D} is the data-driven operator. Then we can generate the feasible set \mathcal{X} of the lower-level problem, i.e. $\mathcal{X} = \{\mathbf{x} | \mathbf{P}\mathbf{F}\mathbf{x} = \bar{\mathbf{y}}, \nabla \mathbf{x} + \mathbf{s}_1 - \mathbf{w} = 0, \nabla \mathbf{x} - \mathbf{s}_2 + \mathbf{w} = 0, \langle \mathbf{e}, \mathbf{w} \rangle + r - \bar{t} = 0, \mathbf{s}_1, \mathbf{s}_2, r \geq 0\}$, where $\bar{\mathbf{y}} = \mathbf{P}\mathbf{F}\bar{\mathbf{x}}$ for any given $\bar{\mathbf{x}} \in \mathcal{X}$, $\mathbf{s}_1, \mathbf{s}_2, r, \mathbf{w}$ are auxiliary variables, $\lambda_{\mathbf{x}}, \lambda_{\mathbf{s}_1}, \lambda_{\mathbf{s}_2}, \lambda_r$ are the corresponding dual multipliers. Based on this feasible set, by introducing auxiliary variable \mathbf{z} , the proximal ADMM updating summarized as:

$$\begin{cases} [\mathbf{z}^{k+1}]_i = \text{sign}([\mathbf{u}^k]_i) \max \left\{ 0, \left| [\mathbf{u}^k]_i \right| - \frac{\rho}{\beta + \tau} \right\}, \\ [\mathbf{s}_1^{k+1}]_i = \max \left\{ 0, \frac{\beta([\mathbf{w}^k]_i - [\nabla \mathbf{x}^k]_i) - [\lambda_{\mathbf{s}_1}^k]_i + \tau[\mathbf{s}_1^k]_i}{\beta + \tau} \right\}, \\ [\mathbf{s}_2^{k+1}]_i = \max \left\{ 0, \frac{\beta([\mathbf{w}^k]_i + [\nabla \mathbf{x}^k]_i) + [\lambda_{\mathbf{s}_2}^k]_i + \tau[\mathbf{s}_2^k]_i}{\beta + \tau} \right\}, \\ r^{k+1} = \max \left\{ 0, \frac{\beta(\bar{t} - \langle \mathbf{e}, \mathbf{w}^k \rangle) - \lambda_r^k + \tau r^k}{\beta + \tau} \right\}, \\ \mathbf{w}^{k+1} = ((2\beta + \tau)\mathbf{I} + \beta \mathbf{e}\mathbf{e}^\top)^{-1} \mathbf{c}^k, \\ \mathbf{x}^{k+1} = (\beta \mathbf{F}^\top \mathbf{P}^\top \mathbf{P} \mathbf{F} + (\eta + \tau)\mathbf{I} + 2\beta \nabla^\top \nabla + \beta \mathbf{T}^\top \mathbf{T})^{-1} \mathbf{d}^k, \\ \lambda_{\mathbf{x}}^{k+1} = \lambda_{\mathbf{x}}^k + \beta(\mathbf{P}\mathbf{F}\mathbf{x}^{k+1} - \bar{\mathbf{y}}), \\ \lambda_{\mathbf{z}}^{k+1} = \lambda_{\mathbf{z}}^k + \beta(\mathbf{z}^{k+1} - \mathbf{T}\mathbf{x}^{k+1}), \\ \lambda_{\mathbf{s}_1}^{k+1} = \lambda_{\mathbf{s}_1}^k + \beta(\nabla \mathbf{x}^{k+1} + \mathbf{s}_1^{k+1} - \mathbf{w}^{k+1}), \\ \lambda_{\mathbf{s}_2}^{k+1} = \lambda_{\mathbf{s}_2}^k + \beta(\nabla \mathbf{x}^{k+1} - \mathbf{s}_2^{k+1} + \mathbf{w}^{k+1}), \\ \lambda_r^{k+1} = \lambda_r^k + \beta(\langle \mathbf{e}, \mathbf{w}^{k+1} \rangle + r^{k+1} - \bar{t}), \end{cases}$$

where $\beta, \tau > 0$ are respectively the penalty and regularization parameters, $\text{sign}(\cdot)$ denotes the sign function, \mathbf{z} is an additional auxiliary variable for the nonconvex upper-level subproblem, $\lambda_{\mathbf{z}}$ is the corresponding dual multiplier, $\mathbf{u}^k = \frac{\beta \mathbf{T}\mathbf{x}^k - \lambda_{\mathbf{z}}^k + \tau \mathbf{z}^k}{\beta + \tau}$, $\mathbf{c}^k = \beta \mathbf{s}_1^{k+1} + \lambda_{\mathbf{s}_1}^k + \beta \mathbf{s}_2^{k+1} - \lambda_{\mathbf{s}_2}^k + (\beta \bar{t} - \beta r^{k+1} - \lambda_r^k) \mathbf{e} + \tau \mathbf{w}^k$, and $\mathbf{d}^k = \beta \mathbf{F}^\top \mathbf{P}^\top \bar{\mathbf{y}} + \eta \mathcal{D}(\mathbf{y}) - \mathbf{F}^\top \mathbf{P}^\top \lambda_{\mathbf{x}}^k + \nabla^\top (\beta(\mathbf{s}_2^{k+1} - \lambda_{\mathbf{s}_2}^k) - \beta(\mathbf{s}_1^{k+1} + \lambda_{\mathbf{s}_1}^k)) + \beta \mathbf{T}^\top \mathbf{z}^{k+1} + \mathbf{T}^\top \lambda_{\mathbf{z}}^k + \tau \mathbf{x}^k$.

REFERENCES

- [1] K. H. Jin, M. T. McCann, E. Froustey, and M. Unser, "Deep convolutional neural network for inverse problems in imaging," *IEEE Trans. Image Process.*, vol. 26, no. 9, pp. 4509–4522, 2017.
- [2] S. Lunz, C. Schoenlieb, and O. Öktem, "Adversarial regularizers in inverse problems," in *Proc. Advances in Neural Inf. Process. Systems*, 2018, pp. 8516–8525.
- [3] C. Li, W. Yin, H. Jiang, and Y. Zhang, "An efficient augmented lagrangian method with applications to total variation minimization," *Computational Optimization and Applications*, vol. 56, no. 3, pp. 507–530, 2013.
- [4] S. A. Bigdeli, M. Zwicker, P. Favaro, and M. Jin, "Deep mean-shift priors for image restoration," in *Proc. Advances in Neural Inf. Process. Systems*, 2017, pp. 763–772.

- [5] N. Yair and T. Michaeli, "Multi-scale weighted nuclear norm image restoration," in *Proc. IEEE Conf. Comput. Vis. Pattern Recognit.*, 2018, pp. 3165–3174.
- [6] Z. Hui, X. Wang, and X. Gao, "Fast and accurate single image super-resolution via information distillation network," in *Proc. IEEE Conf. Comput. Vis. Pattern Recognit.*, 2018, pp. 723–731.
- [7] D. Liu, B. Wen, Y. Fan, C. C. Loy, and T. S. Huang, "Non-local recurrent network for image restoration," in *Proc. Advances in Neural Inf. Process. Systems*, 2018, pp. 1680–1689.
- [8] Y. Zhang, K. Li, K. Li, B. Zhong, and Y. Fu, "Residual non-local attention networks for image restoration," in *International Conference on Learning Representations*, 2019.
- [9] K. Li and J. Malik, "Learning to optimize," in *International Conference on Learning Representations*, 2017.
- [10] R. Liu, S. Cheng, L. Ma, X. Fan, Z. Luo *et al.*, "A bridging framework for model optimization and deep propagation," in *Proc. Advances in Neural Inf. Process. Systems*, 2018, pp. 4323–4332.
- [11] K. Zhang, W. Zuo, S. Gu, and L. Zhang, "Learning deep cnn denoiser prior for image restoration," in *Proc. IEEE Conf. Comput. Vis. Pattern Recognit.*, 2017, pp. 3929–3938.
- [12] R. Liu, S. Cheng, L. Ma, X. Fan, and Z. Luo, "Deep proximal unrolling: Algorithmic framework, convergence analysis and applications," *IEEE Trans. Image Process*, 2019.
- [13] R. Liu, S. Cheng, Y. He, X. Fan, Z. Lin, and Z. Luo, "On the convergence of learning-based iterative methods for nonconvex inverse problems," *IEEE Trans. Pattern Anal. Mach. Intell.*, 2019.
- [14] S. Dempe, V. Kalashnikov, G. A. Prez-Valds, and N. Kalashnykova, *Bilevel Programming Problems: Theory, Algorithms and Applications to Energy Networks*. Springer Publishing Company, Incorporated, 2015.
- [15] M. Solodov, "An explicit descent method for bilevel convex optimization," *Journal of Convex Analysis*, vol. 14, no. 2, p. 227, 2007.
- [16] A. Beck and S. Sabach, "A first order method for finding minimal norm-like solutions of convex optimization problems," *Mathematical Programming*, vol. 147, no. 1-2, pp. 25–46, 2014.
- [17] S. Sabach and S. Shtern, "A first order method for solving convex bilevel optimization problems," *SIAM Journal on Optimization*, vol. 27, no. 2, pp. 640–660, 2017.
- [18] E. M. Eksioğlu, "Decoupled algorithm for mri reconstruction using nonlocal block matching model: Bm3d-mri," *J MATH IMAGING VIS*, vol. 56, no. 3, pp. 430–440, 2016.
- [19] M. Haris, G. Shakhnarovich, and N. Ukita, "Deep back-projection networks for super-resolution," in *Proc. IEEE Conf. Comput. Vis. Pattern Recognit.*, 2018, pp. 1664–1673.
- [20] X. Tao, H. Gao, X. Shen, J. Wang, and J. Jia, "Scale-recurrent network for deep image deblurring," in *Proc. IEEE Conf. Comput. Vis. Pattern Recognit.*, 2018, pp. 8174–8182.
- [21] X. Wang, R. Girshick, A. Gupta, and K. He, "Non-local neural networks," in *Proc. IEEE Conf. Comput. Vis. Pattern Recognit.*, 2018, pp. 7794–7803.
- [22] E. Agustsson and R. Timofte, "Ntire 2017 challenge on single image super-resolution: Dataset and study," in *Proc. IEEE Conf. Comput. Vis. Pattern Recognit. Workshops*, 2017.
- [23] K. He, X. Zhang, S. Ren, and J. Sun, "Deep residual learning for image recognition," in *Proc. IEEE Conf. Comput. Vis. Pattern Recognit.*, 2016, pp. 770–778.
- [24] K. He, G. Gkioxari, P. Dollár, and R. Girshick, "Mask r-cnn," in *Proc. IEEE Conf. Int. Conf. Comput. Vis.*, 2017, pp. 2980–2988.
- [25] L. Fan, W. Huang, C. Gan, S. Ermon, B. Gong, and J. Huang, "End-to-end learning of motion representation for video understanding," in *Proc. IEEE Conf. Comput. Vis. Pattern Recognit.*, 2018, pp. 6016–6025.
- [26] J. Zhang and B. Ghanem, "Ista-net: Interpretable optimization-inspired deep network for image compressive sensing," in *Proc. IEEE Conf. Comput. Vis. Pattern Recognit.*, 2018, pp. 1828–1837.
- [27] J. Sun, H. Li, Z. Xu *et al.*, "Deep admn-net for compressive sensing mri," in *Proc. Advances in Neural Inf. Process. Systems*, 2016, pp. 10–18.
- [28] S. Dempe, "Bilevel optimization: theory, algorithms and applications," *Optimization On-line* URL http://www.optimization-online.org/DB_HTML/2018/08/6773.html, 2018.
- [29] J. Wright, A. Y. Yang, A. Ganesh, S. S. Sastry, and Y. Ma, "Robust face recognition via sparse representation," *IEEE Trans. Pattern Anal. Mach. Intell.*, vol. 31, no. 2, pp. 210–227, 2009.
- [30] M.-M. Cheng, N. J. Mitra, X. Huang, P. H. Torr, and S.-M. Hu, "Global contrast based salient region detection," *IEEE Trans. Pattern Anal. Mach. Intell.*, vol. 37, no. 3, pp. 569–582, 2015.
- [31] R. Liu, L. Ma, Y. Wang, and L. Zhang, "Learning converged propagations with deep prior ensemble for image enhancement," *IEEE Trans. Image Process*, vol. 28, no. 3, pp. 1528–1543, 2019.
- [32] A. L. Dontchev and R. T. Rockafellar, "Implicit functions and solution mappings," *Springer Monogr. Math.*, 2009.
- [33] R. G. Baraniuk, "Compressive sensing," *IEEE Signal Processing Magazine*, vol. 24, no. 4, 2007.
- [34] A. Levin, Y. Weiss, F. Durand, and W. T. Freeman, "Understanding and evaluating blind deconvolution algorithms," in *Proc. IEEE Conf. Comput. Vis. Pattern Recognit.*, 2009, pp. 1964–1971.
- [35] J. M. Bioucas-Dias and M. A. Figueiredo, "A new twist: two-step iterative shrinkage/thresholding algorithms for image restoration," *IEEE Trans. Image Process*, vol. 16, no. 12, pp. 2992–3004, 2007.
- [36] K. Zhang, W. Zuo, and L. Zhang, "Learning a single convolutional super-resolution network for multtrans. image processle degradations," in *Proc. IEEE Conf. Comput. Vis. Pattern Recognit.*, 2018, pp. 3262–3271.
- [37] O. Russakovsky, J. Deng, H. Su, J. Krause, S. Satheesh, S. Ma, Z. Huang, A. Karpathy, A. Khosla, M. Bernstein, A. C. Berg, and L. Fei-Fei, "Imagenet large scale visual recognition challenge," *International Journal of Computer Vision*, vol. 115, no. 3, pp. 211–252, 2015.
- [38] A. Beck and M. Teboulle, "A fast iterative shrinkage-thresholding algorithm for linear inverse problems," *SIAM journal on imaging sciences*, vol. 2, no. 1, pp. 183–202, 2009.
- [39] D. Krishnan and R. Fergus, "Fast image deconvolution using hyper-laplacian priors," in *Proc. Advances in Neural Inf. Process. Systems*, 2009, pp. 1033–1041.
- [40] A. Danielyan, V. Katkovich, and K. Egiazarian, "Bm3d frames and variational image deblurring," *IEEE Trans. Image Process*, vol. 21, no. 4, pp. 1715–1728, 2012.
- [41] D. Zoran and Y. Weiss, "From learning models of natural image patches to whole image restoration," in *Proc. IEEE Conf. Comput. Vis. Pattern Recognit.*, 2011, pp. 479–486.
- [42] C. J. Schuler, H. C. Burger, S. Harmeling, and B. Scholkopf, "A machine learning approach for non-blind image deconvolution," in *Proc. IEEE Conf. Comput. Vis. Pattern Recognit.*, 2013, pp. 1067–1074.
- [43] M. Lustig, D. L. Donoho, J. M. Santos, and J. M. Pauly, "Compressed sensing mri," *IEEE SIGNAL PROCESSING MAGAZINE*, vol. 25, no. 2, pp. 72–82, 2008.
- [44] X. Qu, D. Guo, B. Ning, Y. Hou, Y. Lin, S. Cai, and Z. Chen, "Undersampled mri reconstruction with patch-based directional wavelets," *MAGN RESON IMAGING*, vol. 30, no. 7, pp. 964–977, 2012.
- [45] X. Qu, Y. Hou, F. Lam, D. Guo, J. Zhong, and Z. Chen, "Magnetic resonance image reconstruction from undersampled measurements using a patch-based nonlocal operator," *MED IMAGE ANAL*, vol. 18, no. 6, pp. 843–856, 2014.
- [46] Z. Zhan, J.-F. Cai, D. Guo, Y. Liu, Z. Chen, and X. Qu, "Fast multiclass dictionaries learning with geometrical directions in mri reconstruction," *IEEE Trans. Biomed. Engineering*, vol. 63, no. 9, pp. 1850–1861, 2016.
- [47] R. Liu, Y. Zhang, S. Cheng, X. Fan, and Z. Luo, "A theoretically guaranteed deep optimization framework for robust compressive sensing mri," in *Proceedings of Association for the Advancement of Artificial Intelligence*, 2019.
- [48] B. He, L.-Z. Liao, D. Han, and H. Yang, "A new inexact alternating directions method for monotone variational inequalities," *Mathematical Programming*, vol. 92, no. 1, pp. 103–118, 2002.
- [49] X. Yuan, S. Zeng, and J. Zhang, "Discerning the linear convergence of admn for structured convex optimization through the lens of variational analysis," *Optimization Online Preprint*, 2018.
- [50] J. F. Bonnans and A. Shapiro, *Perturbation analysis of optimization problems*. Springer Science & Business Media, 2013.